Current-to-Frequency Converter Based Photometer Circuit

Wilmar Hernandez, *Senior Member, IEEE*, Alfredo Mendez, Vicente González-Posadas, José Luis Jiménez-Martín, and Francisco José Arqués-Orobón

***Abstract*— In this article, the design of a photometer circuit based on a current-to-frequency converter is presented. This circuit is a piecewise linear circuit that makes the most of feedback to ensure a linear relationship between the input photocurrent and the output frequency. Here, Proteus simulations were used to verify the performance of the proposed circuit, and the electronic simulations and the experimental results were shown to be in total agreement. The experimental results showed that the proposed circuit rejected better additive white Gaussian noise signals than the classic photometer circuit based on the transimpedance amplifier. In addition, despite that the proposed circuit is more complex than the classic one, its high linearity, noise rejection, and easy implementation make it suitable for applications where measurement precision and noise rejection are of paramount importance.**

***Index Terms*— Current-to-frequency converter (CFC), current-to-voltage converter (CVC), photometer circuit, relative proximity coefficient, transimpedance amplifier.**

I. Introduction

OPTOELECTRONIC devices transform light energy into electrical energy or vice versa, connecting optical systems with electronic systems. In this way, researchers and engineers design instruments to generate, detect, and/or control light in many applications of science and engineering put at the service of society. Some optoelectronic devices of great importance today are the following: solar cells, photodiodes, phototransistors, photoresistors, photomultiplier tubes, charge-coupled imaging devices, laser diodes, and light-emitting diodes, among others. In addition, these devices can be found as part of medical and military equipment, and telecommunication and automatic control systems, among others [1]–[7].

Manuscript received November 20, 2021; revised December 28, 2021; accepted January 9, 2022. Date of publication January 19, 2022; date of current version March 2, 2022. This work was supported in part by the Corporación Ecuatoriana para el Desarrollo de la Investigación y la Academia (CEDIA), Ecuador, under Research Project CEPRA XII-2018-13, in part by the Universidad de Las Américas (UDLA), Quito, Ecuador, under Research Project IEA.WHP.21.02, and in part by the Universidad Politécnica de Madrid (UPM), Spain. The Associate Editor coordinating the review process was Alvaro Hernandez. *(Corresponding author: Wilmar Hernandez.)*

Wilmar Hernandez is with the Facultad de Ingeniería y Ciencias Aplicadas, Universidad de Las Américas, Quito 170504, Ecuador (e-mail: wilmar.hernandez@udla.edu.ec).

Alfredo Mendez is with the Departamento de Matemática Aplicada a las Tecnologías de la Información y Comunicaciones, ETSIS de Telecomunicación, Universidad Politécnica de Madrid, 28031 Madrid, Spain (e-mail: alfredo.mendez@upm.es).

Vicente González-Posadas, José Luis Jiménez-Martín, and Francisco José Arqués-Orobón are with the Departamento de Ingeniería Audiovisual Comunicaciones, ETSIS de Telecomunicación, Universidad Politécnica de Madrid, 28031 Madrid, Spain (e-mail: vicente.gonzalez@upm.es; joseluis.jimenez@upm.es; jose.arques@upm.es).

Digital Object Identifier 10.1109/TIM.2022.3144746

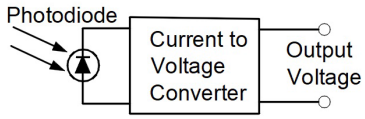

Fig. 1. Classic photometer circuit general schematic: photometer based on a photodiode operating in the photovoltaic mode and coupled to a CVC.

In this research, a photometer circuit whose sensor element is a photodiode operating in photovoltaic mode is presented [1], [8], [9]. In this operation mode, both the voltage across the photodiode and the dark current flowing through it are zero. In addition, the noise level is low, and both sensitivity and linearity are high. The active version of the photovoltaic mode circuit implementation, where applications prioritize precision over speed, is a current-to-voltage converter (CVC) based on a transimpedance amplifier [10].

The general idea behind the classic photometer schematic shown in Fig. 1, based on the photodiode operating in photovoltaic mode and coupled to a transimpedance amplifier, has found many practical applications [11]–[18]. However, despite the advantages that were mentioned in previous paragraphs, especially the low noise and the output voltage that vary linearly with respect to the photodiode current (i.e., the short-circuit current), the rejection of the photometer circuit to additive noise that contaminates the input signal can be improved. In short, it is important to improve the response of the circuit to this type of noise because, when the input noise is white noise, it is very difficult to eliminate its contribution to the output voltage. This is because the power spectral density of this type of noise is constant, the signal contains all frequencies, and, in practice, all frequencies show power values other than zero [19], [20].

Therefore, in order to increase the level of noise rejection, guaranteeing high linearity, in this article, a photometer circuit based on a current-to-frequency converter (CFC) (see Fig. 2) is proposed. Here, as in the classic case, the photodiode is operating in the photovoltaic mode, but, unlike the classic case, now, the output is a pulse train whose frequency varies linearly with respect to the photodiode current. In addition, as the output variables of each of the circuits are different, a coefficient, called the relative proximity coefficient, has been devised to be able to compare how much the response of each photometer deviates from the value that it would have for an input signal without noise and the same input signal but with added noise.

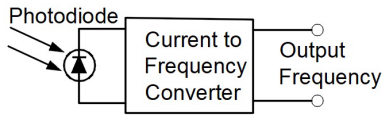

Fig. 2. Proposed photometer circuit general schematic: photometer based on a photodiode operating in the photovoltaic mode and coupled to a CFC.

The proposed photometer circuit is more complex than the classic circuit because the new circuit is designed by connecting both linear and nonlinear stages, among other things. Nevertheless, the proposed circuit is easy to implement. Furthermore, the different values taken by the relative proximity coefficient for each of the circuits, as a function of the input noise level, showed that the noise rejection level of the proposed circuit was much higher than the noise rejection level of the classic circuit. The noise that affects the behavior of the sensors has been studied extensively over the years from different points of view because it corrupts the measurements and generates uncertainty in the measurement systems [21]. Therefore, it has always been a challenge for electronic engineers to design high-performance circuits that are as immune as possible to this type of unwanted signal [22], [23].

The proposed photometer circuit is presented in Section II. The objective of Section III is to carry out the comparison between the performance of the proposed photometer circuit and the classic photometer circuit based on a transimpedance amplifier. Moreover, Section IV is aimed at the discussion of the results. Finally, Section V presents the conclusions of this article.

II. Proposed Photometer Circuit

A circuit implementation of Fig. 1 is shown in Fig. 3. The feedback network shown in Fig. 3(a) can be as complex as the design allows. However, in general, it is typical for it to be formed by a resistor, or in the event that frequency compensation is required to avoid instability problems of the transimpedance amplifier, a low-value capacitor is placed in parallel with the feedback resistor to reduce the transimpedance value at high frequency. In addition, there are configurations in which the equivalent feedback resistance is represented as the connection of resistors in series or in parallel or neither in series nor in parallel, together with compensating capacitors [1], [8], [9].

In the case under study, the feedback network consists of a single compensation resistor [see Fig. 3(b)] because, due to the characteristics of the input signal, there are no instability problems, and the step output ringing and gain peaking do not affect the output signal. In Fig. 3(b), R_f is the feedback resistor, and the photodiode circuit model is represented by the following elements: photodiode current generated by the incident light (i_P), series resistance (R_S), junction capacitance (C_J), and junction shunt resistance (R_{SH}).

Fig. 4 shows the schematic that represents in detail what is shown in Fig. 2. The idea behind Fig. 4 is the one that supported the photometer circuit proposed in this article and shown in Fig. 5. The transfer function of the proposed circuit is given as follows:

$$H(s) = \frac{F(s)}{I_P(s)} = \frac{E_1 B_1 C_{H1}}{A_6 C_{H2}\left(\frac{A_3}{A_6}s^3 + \frac{A_4}{A_6}s^2 + \frac{A_5}{A_6}s + 1\right)} \tag{1}$$

where $H(s) = \mathcal{L}\{h(t)\}$ is the Laplace transform of the impulse response, $h(t)$, of this system, $I_P(s) = \mathcal{L}\{i_P(t)\}$ is the Laplace transform of the photodiode current, and $F(s) = \mathcal{L}\{f(t)\}$ is the Laplace transform of the output frequency. In short, $H(s)$ (i.e., the transfer function) is the linear mapping of $I_P(s)$ to $F(s)$. Here, $i_P(t)$ and $f(t)$ are continuous-time signals. In addition, the coefficients of the numerator and the denominator of (1) are given as follows:

$$A_1 = R_b R_{\mathrm{SH}} + R_S R_b + R_c R_{\mathrm{SH}} + R_c R_S + R_b R_c \tag{2}$$
$$A_2 = C_J R_{\mathrm{SH}}(R_S R_b + R_S R_c + R_b R_c) \tag{3}$$
$$A_3 = A_2 C_2 L R_0 \tag{4}$$
$$A_4 = A_1 C_2 L R_0 + A_2 L \tag{5}$$
$$A_5 = A_1 L + A_2 R_0 + C_J R_{\mathrm{SH}} R_S R_b D_1 R_0 G \tag{6}$$
$$A_6 = A_1 R_0 + D_1 R_0 G R_b R_{\mathrm{SH}} + D_1 R_0 G R_S R_b \tag{7}$$
$$B_1 = D_1 R_0 G R_c (R_{\mathrm{SH}} + R_S + R_b) \tag{8}$$
$$C_{H1} = R_b \| R_{\mathrm{SH}} \tag{9}$$
$$C_{H2} = 1 + \frac{R_S}{R_b + R_{\mathrm{SH}}} \tag{10}$$
$$D_1 = \frac{R_5 R_6}{R_4 R_7} \tag{11}$$
$$E_1 = \frac{(R_4 R_7 - R_5 R_6)(R_6 \| R_7) R_{10}}{2 R_4^2 R_7^2 (R_9 \| R_{10}) C_1 V_{\mathrm{OM}}} \tag{12}$$
$$R_b = \frac{R_{f1} R_{f2} + R_{f1} R_{f3} + R_{f2} R_{f3}}{R_{f2}} \tag{13}$$
$$R_c = \frac{R_{f1} R_{f2} + R_{f1} R_{f3} + R_{f2} R_{f3}}{R_{f3}} \tag{14}$$

where G is the open-loop gain of the operational amplifier, V_{OM} is the maximum peak output voltage swing of the operational amplifier, and $\|$ is the parallel operator. In addition, R_0 is the load resistance seen by the LC_2 filter and represents the ability of the circuit to ensure that variations in the load current do not affect the value of the output voltage of the LC_2 filter. Furthermore, operational amplifiers were considered to have high input impedance and low output impedance. Moreover, the different forms that the impulse response of the system $h(t)$ could have, for the transfer function given by (1), are shown in the Appendix.

Finally, the output frequency of the circuit shown in Fig. 5 is given as follows:

$$f(t) = (h * i_P)(t) = \int_0^t h(t-\tau) i_P(\tau)\, d\tau \tag{15}$$

where the symbol $*$ is the convolution operator and $h, i_P : [0, \infty] \to \mathbb{R}$.

III. Results: Classic Photometer Circuit Versus Proposed Photometer Circuit

As in previous research [24]–[26], the silicon photodiode BPW21 [27] was used in this article with $R_S = 1\ \Omega$, $R_{\mathrm{SH}} = 100\ \mathrm{M}\Omega$, and $C_J = 580$ pF for 0 V applied across the

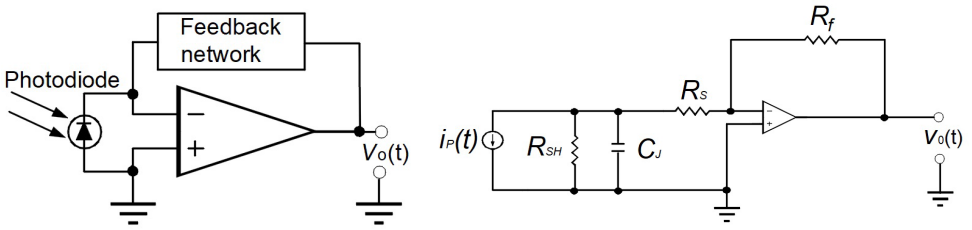

Fig. 3. Classic photometer circuit. (a) Photodiode amplifier operating in the photovoltaic mode. (b) Circuit implementation of the classic photodiode amplifier operating in the photovoltaic mode.

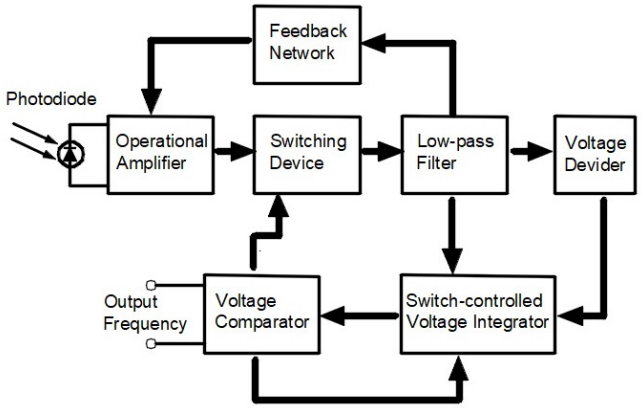

Fig. 4. Specific schematic of the proposed photometer circuit.

BPW21. In [24]–[26], the RS Stock No. 194-004 Modulated Laser Diode Module (maximum power output = 3 mW and nominal wavelength = 670 nm) was used to generate the incident light, and a polarizer was used to generate different values of incident light power. The experimental sensitivity of this photodiode at 670 nm was equal to 0.1345 A/W [24]–[26].

In this research, the photometer circuits were implemented by using the TL084 operational amplifier [28], and the components used in the circuits of Figs. 3(b) and 5 were the following: $R_f = 24.783$ kΩ, $R_{f1} = R_{f2} = R_6 = R_7 = R_{10} = 10$ kΩ, $R_{f3} = 100$ kΩ, $R_4 = 6$ kΩ, $R_5 = 3$ kΩ, $R_8 = R_{11} = 1$ kΩ, $R_9 = 5$ kΩ, $C_1 = 10$ nF, $C_2 = 1000$ μF, $L = 10$ mH, D is the 1N4148 diode, and Q_1 and Q_2 are the 2N7002K MOSFETs. In addition, $V_1 = 2.5$ V, and the supply voltage of the operational amplifiers was ±15 V.

A. Impulse Response of the Proposed Photometer Circuit

For the electronic components mentioned above, the stability of the system is determined by the value of R_0, which turned out to be very small, because, in steady state, for a constant incident light power, the voltage drop at the output of the LC_2 filter also remains practically constant. Now, the closed-loop transfer function (1) can be written as a function of R_0, and considering the typical value of the open-loop voltage gain of the TL084 operational amplifier, which is $G = 125$ dB [28], this transfer function is given as follows:

$$H(s) = \frac{\frac{K_1 K_8}{K_7}}{\frac{K_2}{K_7}s^3 + \left(\frac{K_3 + \frac{K_4}{R_0}}{K_7}\right)s^2 + \left(\frac{K_5 + \frac{K_6}{R_0}}{K_7}\right)s + 1} \quad (16)$$

where $K_1 = 1.0522050105 \cdot 10^{12}$, $K_2 = 2.55793398 \cdot 10^3$, $K_3 = 2.3104410231 \cdot 10^8$, $K_4 = 2.55793398 \cdot 10^6$, $K_5 = 1.108551500513704 \cdot 10^{10}$, $K_6 = 2.3104410231 \cdot 10^{11}$, $K_7 = 1.867195709653826 \cdot 10^{19}$, and $K_8 = 9.490938499459141 \cdot 10^7$. For these values, it can be shown that the closed-loop transfer function (16) is stable for $R_0 \in (0, 4.12\ \text{m}\Omega)$.

Next, the value of R_0 will be found by electronic simulation, using Proteus 8.11 simulations [29], and taking into account the voltage drop across the C_2 capacitor (see Fig. 5). Electronic circuit simulations are of great importance because they allow designers to understand the behavior of these circuits and study their response to different types of input signals [30]–[32]. The transfer function from the photocurrent ($i_P(t)$) to the voltage drop across C_2 ($v_{C_2}(t)$) is given as follows:

$$M(s) = \frac{V_{C_2}(s)}{I_P(s)} = \frac{\frac{K_1 R_b R_{\text{SH}}}{K_7(R_b + R_{\text{SH}} + R_S)}}{\frac{K_2}{K_7}s^3 + \left(\frac{K_3 + \frac{K_4}{R_0}}{K_7}\right)s^2 + \left(\frac{K_5 + \frac{K_6}{R_0}}{K_7}\right)s + 1} \quad (17)$$

where $R_b = 210$ kΩ [see (13)].

At this point, it is important to mention that, to find R_0, the result of the electronic simulation of the voltage drop across C_2 was compared with the results of the MATLAB simulation (MATLAB 2019b [33]) of (17) for a 403.5-μA photocurrent step input. This photocurrent value corresponds to an incident light power equal to 3 mW since the sensitivity of the photodiode is 0.1345 A/W.

In short, to find R_0, the smallest possible value of the square of the two-norm of the difference between step-response characteristics of both types of simulations ($||\Delta||_2^2$) was found. The step-response characteristics of the voltage drop across C_2 that was considered are the following: 1) rise time; 2) transient time; 3) settling time; 4) minimum value of the voltage drop once the response has risen; 5) maximum value of the voltage drop once the response has risen; 6) overshoot; 7) undershoot; 8) peak value; and 9) peak time. The result of this comparison was that the minimum value of $||\Delta||_2^2$ was $||\Delta||_{2\text{min}}^2 = 0.032115$, and it was achieved at $R_0 = 90$ nΩ. Fig. 6 shows the 2-D line plot of the data in $||\Delta||_2^2$ versus the corresponding values in R_0, around the minimum value ($||\Delta||_{2\text{min}}^2$). Furthermore, Fig. 7 shows the curves using MATLAB simulation and Proteus simulation. The difference between both curves is due to the fact that one is the result of a linear system [MATLAB simulation of (17)], and the other is the result of a piecewise linear system

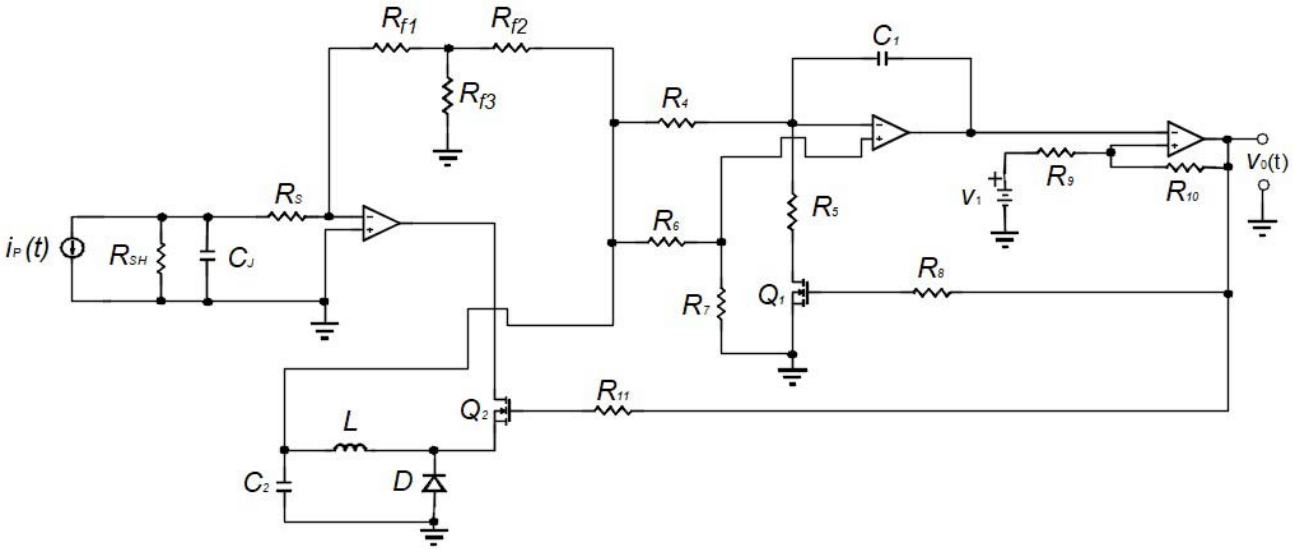

Fig. 5. Proposed photometer circuit.

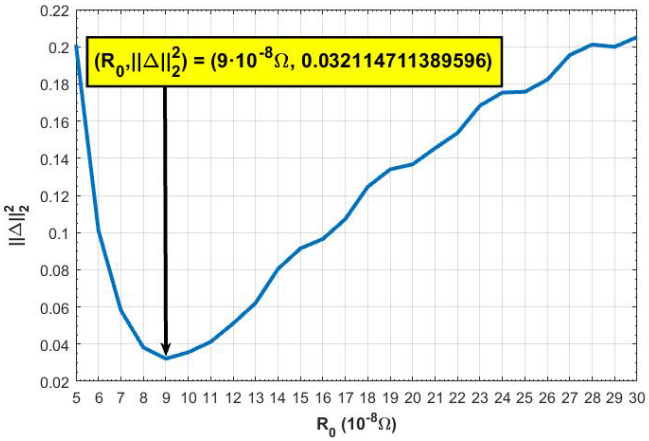

Fig. 6. 2-D line plot of the data in $||\Delta||_2^2$ versus the corresponding values in R_0.

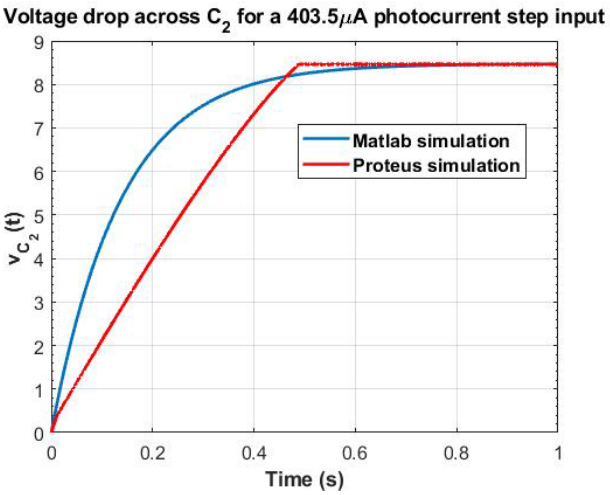

Fig. 7. Voltage drop across C_2 for $i_P(t) = 403.5u(t)$ μA, where $u(t)$ is the unit step function.

(Proteus simulation of the circuit shown in Fig. 5), which includes nonlinear devices, such as voltage comparators.

Taking into account the results shown above, it can be said that the impulse response of the proposed photometer circuit has the form of (29) and is given as follows:

$$h(t) = 9.5 \cdot 10^6 \cdot \Big[7.7 \cdot 10^{-14} \cdot e^{-1.1 \cdot 10^{10} t} - \swarrow \\ \hookrightarrow -9.5 \cdot 10^{-9} \cdot e^{-9.0 \cdot 10^4 t} + 9.5 \cdot 10^{-9} \cdot e^{-7.3\ t}\Big] \cdot u(t) \tag{18}$$

where $u(t)$ is the unit step function.

B. Simulation Results

The response of the photometer circuits is shown in Table I. The frequency values shown in Table I were obtained from the Fourier transform of the output pulse train of the circuit. In addition, for the classic photometer circuit, the linear fit of data is shown in Fig. 8. Furthermore, the linear fit of data for the proposed photometer circuit is shown in Fig. 9. These figures show that both circuits are linear. This is confirmed by the value of the linear correlation coefficient (ρ) between the input and output variables of the curves shown in Figs. 8 and 9. In this case, ρ can be used as a measure of the linear association that exists between the input and output variables [34]. For the classic circuit, $\rho = \rho_{cc} = 1$; for the proposed circuit, $\rho = \rho_{pc} = 0.999782$.

As expected, the performance of the classic circuit is more linear than the one of the proposed circuits because, in the second case, the circuit was designed by connecting both linear and nonlinear stages. Anyway, it is worth mentioning that a linear regression line would explain approximately 100% (ρ_{cc}^2) of the total variation of the output voltage of the classic circuit and approximately 99.9563% (ρ_{pc}^2) of the total variation of the output frequency of the proposed circuit [34].

At this point, it is important to mention that the photocurrent values that were used to make the comparison between the performance of the photometer circuits, through

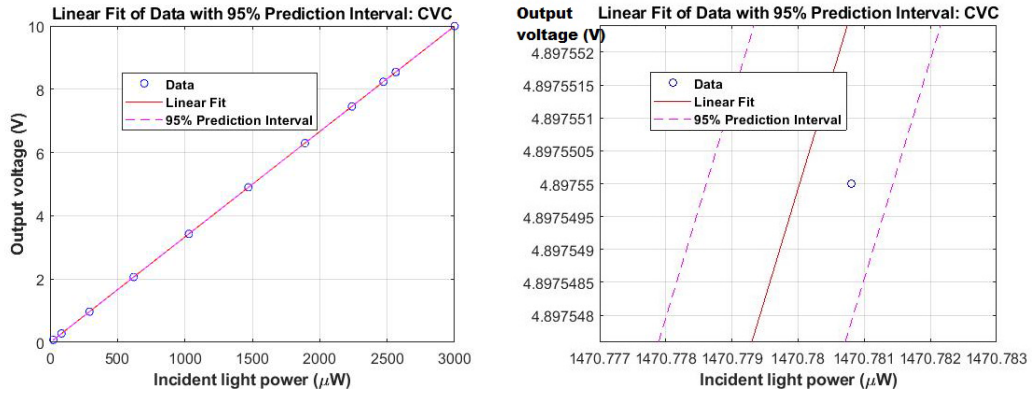

(a) (b)

Fig. 8. Classic photometer circuit (Proteus 8.11 simulation). Photometer circuit based on the CVC: original data, linear fit, and 95% prediction interval. (a) Linear fit of data. (b) Zoomed-in view on the linear fit of data.

TABLE I

RESPONSE OF THE PHOTOMETER CIRCUITS (PROTEUS 8.11 SIMULATION): CVC—PHOTOMETER CIRCUIT BASED ON THE CVC (CLASSIC PHOTOMETER CIRCUIT) AND CFC—PHOTOMETER CIRCUIT BASED ON THE CFC (PROPOSED PHOTOMETER CIRCUIT)

Incident light power (μW)	CVC Output voltage (V)	CFC Output frequency (Hz)
24.09	0.08	19.31
85.51	0.28	101.33
292.68	0.97	374.76
620.62	2.06	784.48
1029.77	3.43	1302.25
1470.78	4.90	1853.74
1890.47	6.30	2377.58
2238.20	7.46	2724.30
2472.05	8.24	3125.05
2563.80	8.54	3185.32
3000.00	10.00	3731.12

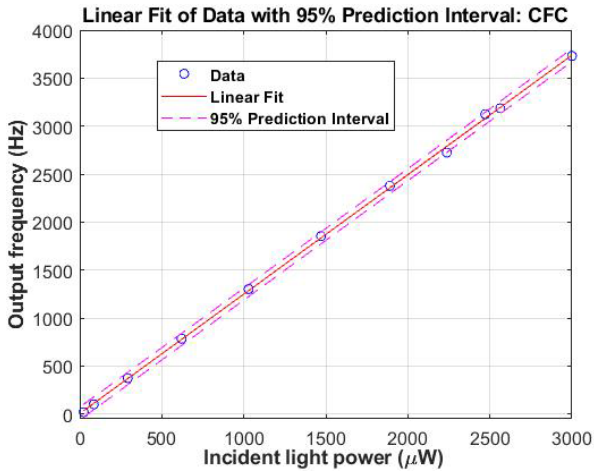

Fig. 9. Proposed photometer circuit (Proteus 8.11 simulation). Photometer circuit based on the CFC: Original data, linear fit, and 95% prediction interval.

Proteus simulations, were chosen taking into account the value of the experimental sensitivity of the BPW21 photodiode (0.1345 A/W) [24]–[26] and the maximum power of the incident light (see Table I).

Finally, although this research is not aimed at carrying out reliability studies of electronic circuits, it could be interesting to have a preliminary idea, at least at the simulation level, on how both photometer circuits behave when the ambient temperature (T_A), for example, is not $T_A = 25\ ^\circ$C. To this end, and to be able to compare the response of both photometers, the relative temperature coefficient of the output of the circuits given by (19) was devised

$$\alpha_T = \frac{1}{\Phi_{25}} \cdot \frac{\text{diff}(\Phi)}{\text{diff}(T)} \tag{19}$$

where T is a vector containing m increasingly distributed temperature values, Φ is a vector of length m whose ith element [i.e., $\Phi(i)$] is the value of the response of the circuit for the ith value of ambient temperature considered, $\Phi_{25} = \Phi(25\ ^\circ\text{C})$, $\text{diff}(\Phi(i)) = \Phi(i) - \Phi(i-1)$, $\text{diff}(T(i)) = T(i) - T(i-1)$, and α_T is a vector of length $m-1$ whose ith element is $\alpha_{\text{Ti}} = (1/\Phi(25\ ^\circ\text{C})) \cdot (\text{diff}(\Phi(i))/\text{diff}(T(i)))$. Fig. 10 shows a plot of α_T versus T of both photometer circuits for an incident light power equal to 24.09 μW and $T = [0\ ^\circ\text{C},\ 5\ ^\circ\text{C},\ 10\ ^\circ\text{C},\ \ldots,\ 50\ ^\circ\text{C}]$.

As expected, Fig. 10 shows that the value of α_T for the classic circuit is smaller than the one of α_T for the proposed circuit. This is because the design of the proposed circuit is much more complex than that of the classic circuit and, therefore, requires as much a greater variety of components as a greater number of components for the implementation of the circuit. This way, what has been said above could explain the reason why the response of the proposed circuit is more affected by temperature variations than the response of the classic circuit.

Finally, it is important to mention that, in Fig. 10, the value of α_T for the classic circuit (α_T^{CVC}) was multiplied by 100 in order to be able to compare it with the value of α_T for the proposed circuit (α_T^{CFC}) using the same 2-D line plot. In view of the results, it can be said that the rejection of both circuits to temperature variations in the interval [0 °C, 50 °C] is satisfactory. Moreover, it is worth noting that, for the chosen analysis interval, the worst case of the relative temperature coefficient of the proposed circuit is $\alpha_T^{\text{CFC}} = 1\ \%/^\circ\text{C}$.

C. Experimental Results

In order to carry out the laboratory tests, the practical assembly of the circuits was carried out both on a printed

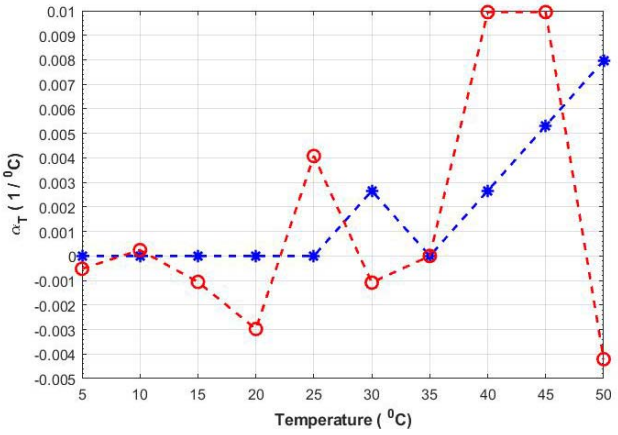

Fig. 10. Relative temperature coefficient (α_T) versus temperature. The response of the classic photometer circuit (CVC) is shown in blue dashed line and $\alpha_T = 100 \cdot \alpha_T^{\text{CVC}}$, where α_T^{CVC} is the value of α_T for the classic circuit, and the response of the proposed photometer circuit (CFC) is shown in red dashed line and $\alpha_T = \alpha_T^{\text{CFC}}$, where α_T^{CFC} is the value of α_T for the proposed circuit.

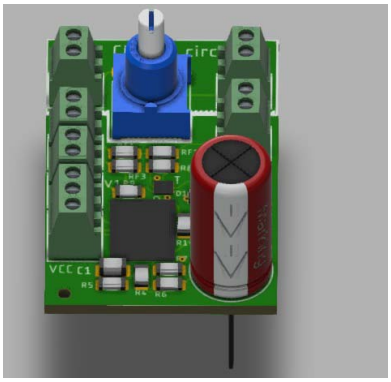

Fig. 11. PCB design of the circuits by using EAGLE. Both circuits were designed on the same PCB.

Fig. 12. Assembly of the circuits. The classic circuit is at the top, and the proposed one is at the bottom.

circuit board (PCB). It is important to mention that these circuits were assembled, in the laboratory, with the same components mentioned above. Fig. 11 shows the PCB, which was designed by using Eagle software [35]. In addition, the components were assembled using solder paste and oven. The assembly of the circuits is shown in Fig. 12.

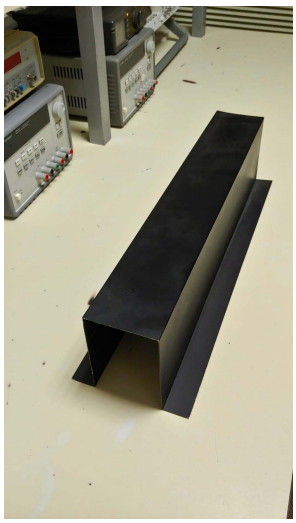

Fig. 13. Tunnel built to carry out measurements.

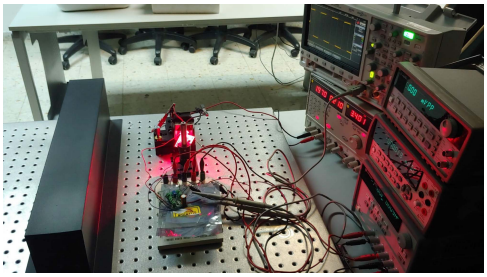

Fig. 14. Workbench: photometer circuits, optical table, measurement equipment, tunnel, and so on.

Unlike the research carried out by the authors previously [24]–[26], in this research, the incident light power was generated by using the NewEnergy High Power LED XQEEPR-00-0000-000000A01-SB01 [36]. In addition, in order to carry out the measurements, the tunnel shown in Fig. 13 was built. Furthermore, Fig. 14 shows the workbench used in this research: optical table, circuits, power LED, power supplies, measurement equipment, and the tunnel. To perform the measurements, both the LED and the photometer circuits were put inside the tunnel. The experimental results are shown in Table II. The output voltage of the classic photometer circuit was measured by using the Agilent 34410A 6 1/2 digit high-performance digital multimeter, and the output frequency of the proposed photometer circuit was measured by using the Agilent Technologies InfiniiVision DSO-X 3024A Digital Oscilloscope. In addition, with the aim of providing measurement accuracy [37] information at least for the main results, the standard error of measurement (SEM) [38] of the classic photometer circuit and the SEM of the proposed photometer circuit are shown in Table II.

As was done in Section III-B, the linear association that exists between the input and output variables was found. From the results shown in Table II, it can be shown that the experimental value of ρ_{cc} is $\rho_{\text{cc}} = 0.999971$, and the experimental value of ρ_{pc} is $\rho_{\text{pc}} = 0.999766$. Therefore, a linear regression line would explain approximately 99.9941% (ρ_{cc}^2) of the total variation of the output voltage of the classic circuit and approximately 99.9533% (ρ_{pc}^2) of the total variation of

TABLE II

EXPERIMENTAL RESULTS: CVC—PHOTOMETER CIRCUIT BASED ON THE CVC (CLASSIC PHOTOMETER CIRCUIT); SEM_{CVC}—STANDARD ERROR OF MEASUREMENT OF THE CVC; CFC—PHOTOMETER CIRCUIT BASED ON THE CFC (PROPOSED PHOTOMETER CIRCUIT); AND SEM_{CFC}—STANDARD ERROR OF MEASUREMENT OF THE CFC

Incident light power (μW)	CVC		CFC	
	Output voltage (V)	SEM_{CVC} (V)	Output frequency (Hz)	SEM_{CFC} (Hz)
24.09	0.1	$0.2 \cdot 10^{-2}$	18.02	$36.17 \cdot 10^{-2}$
85.51	0.29	$0.42 \cdot 10^{-2}$	100.44	$154.73 \cdot 10^{-2}$
292.68	0.95	$0.18 \cdot 10^{-1}$	369.5	$386.8 \cdot 10^{-2}$
620.62	2.1	$3.6 \cdot 10^{-2}$	783	$537 \cdot 10^{-2}$
1029.77	3.46	$3.04 \cdot 10^{-2}$	1307	$4041 \cdot 10^{-4}$
1470.78	4.92	$2.88 \cdot 10^{-2}$	1854	$1674 \cdot 10^{-3}$
1890.47	6.33	$2.78 \cdot 10^{-2}$	2381	$1617 \cdot 10^{-3}$
2238.20	7.44	$9.34 \cdot 10^{-2}$	2726	$7044 \cdot 10^{-3}$
2472.05	8.23	$7.38 \cdot 10^{-2}$	3131	$2309 \cdot 10^{-3}$
2563.80	8.5	$4.0 \cdot 10^{-2}$	3189	$1039 \cdot 10^{-3}$
3000.00	10.04	$19.91 \cdot 10^{-3}$	3731	$2517 \cdot 10^{-3}$

the output frequency of the proposed circuit. This shows that the experimental results are in agreement with the simulation results.

Finally, in order to be able to compare the noise rejection ability of both circuits, the relative proximity coefficient (R_{prox}) was defined as follows.

Definition: Given a photocurrent value determined by the power of the incident light on the photodiode, the relative proximity coefficient is given by

$$R_{\text{prox}} = \left| \frac{\vartheta - \delta}{\vartheta} \right| \tag{20}$$

where $|.|$ is the absolute vale operator, $\vartheta \in \mathbb{R}$ is the value of the output signal when the input photocurrent is not contaminated with noise, and $\delta \in \mathbb{R}$ is the value of the output signal when the input photocurrent is contaminated with additive white Gaussian noise (AWGN).

Remark: For a well-designed circuit, it is always true that $R_{\text{prox}} \to 0$. Therefore, the lower R_{prox}, the higher the noise rejection ability of the circuit.

The way that was devised to measure the noise rejection ability of both circuits consisted of generating an AWGN signal of amplitude 100 mV_{pp}, using the Agilent 33120A 15-MHz function/arbitrary waveform generator, and connecting a 50-Ω resistor in series between the generator output and photodiode cathode. Then, the value of the power of the incident light on the photodiode was increased, and the output values of both circuits were recorded. Table III shows the experimental results of the noise rejection ability test, and the value of the relative proximity coefficient for each circuit is shown in Fig. 15. The relative proximity coefficient was obtained by using (20) and the information given in Tables II and III.

D. Comparison Between Theoretical and Experimental Results

The transfer function of the classic circuit shown in Fig. 3(b) is given by (21), the impulse response has the form of (22)

TABLE III

EXPERIMENTAL RESULTS WITH THE INPUT SIGNAL CONTAMINATED BY AN AWGN SIGNAL OF AMPLITUDE 100 mV_{pp} CONNECTED TO THE CATHODE OF THE PHOTODIODE THROUGH A 50-Ω SERIES RESISTOR: CVC—PHOTOMETER CIRCUIT BASED ON THE CVC (CLASSIC PHOTOMETER CIRCUIT) AND CFC—PHOTOMETER CIRCUIT BASED ON THE CFC (PROPOSED PHOTOMETER CIRCUIT)

Incident light power (μW)	CVC Output voltage (V)	CFC Output frequency (Hz)
24.09	0.36	48.45
85.51	0.59	134
292.68	1.25	398
620.62	2.32	819
1029.77	3.64	1329
1470.78	5.06	1881
1890.47	6.43	2397
2238.20	7.34	2738
2472.05	8.45	3144
2563.80	8.62	3201
3000.00	10.12	3746

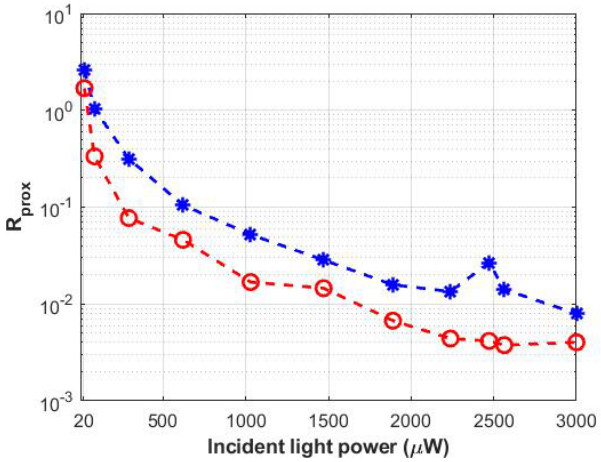

Fig. 15. Relative proximity coefficient (R_{prox}) versus incident light power. The response of the classic photometer circuit (CVC) is shown in blue dashed line, $R_{\text{prox}} = R_{\text{prox}}^{\text{CVC}}$, where $R_{\text{prox}}^{\text{CVC}}$ is the value of R_{prox} for the classic circuit, and the response of the proposed photometer circuit (CFC) is shown in red dashed line and $R_{\text{prox}} = R_{\text{prox}}^{\text{CFC}}$, where $R_{\text{prox}}^{\text{CFC}}$ is the value of R_{prox} for the proposed circuit.

and is given by (25), and the output voltage of this circuit is given by (26)

$$H_{\text{cc}}(s) = \frac{V_0(s)}{I_P(s)} = \frac{\Upsilon}{s + \beta} \tag{21}$$

$$h_{\text{cc}}(t) = \Upsilon e^{-\beta t} u(t) \tag{22}$$

where $H_{\text{cc}}(s) = \mathcal{L}\{h_{\text{cc}}(t)\}$ is the Laplace transform of the impulse response, $h_{\text{cc}}(t)$, of the classic circuit, $I_P(s) = \mathcal{L}\{i_P(t)\}$ is the Laplace transform of the photodiode current, and $V_0(s) = \mathcal{L}\{v_0(t)\}$ is the Laplace transform of the output voltage. In short, $H_{\text{cc}}(s)$ is the linear mapping of $I_P(s)$ to $V_0(s)$. Here, $i_P(t)$ and $v_0(t)$ are continuous-time signals. In addition, the coefficients of the numerator and the denominator of (21) are given as follows:

$$\Upsilon = \frac{R_f}{C_J R_S} \tag{23}$$

$$\beta = \frac{1}{C_J (R_S \| R_{\text{SH}})}. \tag{24}$$

TABLE IV

OUTPUT VALUES OF THE CLASSIC CIRCUIT: THEORETICAL RESULTS BASED ON (26) MULTIPLIED BY THE SENSITIVITY OF THE PHOTODIODE

Incident light power (μW)	Output voltage (V)
24.09	0.08
85.51	0.29
292.68	0.98
620.62	2.07
1029.77	3.43
1470.78	4.90
1890.47	6.30
2238.20	7.46
2472.05	8.24
2563.80	8.55
3000.00	10.00

TABLE V

OUTPUT VALUES OF THE PROPOSED CIRCUIT: THEORETICAL RESULTS BASED ON (15) MULTIPLIED BY THE SENSITIVITY OF THE PHOTODIODE

Incident light power (μW)	Output frequency (Hz)
24.09	30.82
85.51	109.39
292.68	374.40
620.62	793.90
1029.77	1317.29
1470.78	1881.44
1890.47	2418.31
2238.20	2863.13
2472.05	3162.27
2563.80	3279.64
3000.00	3837.76

Therefore,

$$h_{\mathrm{cc}}(t) = 4.273 \cdot 10^{13} \cdot e^{-1.724 \cdot 10^{9} t} \cdot u(t) \tag{25}$$

and

$$v_0(t) = (h_{\mathrm{cc}} * i_P)(t) = \int_0^t h_{\mathrm{cc}}(t-\tau) i_P(\tau)\, d\tau. \tag{26}$$

The theoretical results of the classic photometer circuit are shown in Table IV, and the theoretical results of the proposed photometer circuit are shown in Table V. To obtain these results, all the equations that have been shown in this article, which leads to giving numerical values to (15) and (26), have been used.

Taking into account the information provided in Tables II, IV, and V, when comparing the theoretical output values with the experimental ones, it is obtained that the linear correlation coefficient between the theoretical output and the experimental output of the classic circuit is $\rho_{\mathrm{cc}}^{\mathrm{theo-exp}} = 0.999967$. Similarly, it is also obtained that the linear correlation coefficient between the theoretical output and the experimental output of the proposed circuit is $\rho_{\mathrm{pc}}^{\mathrm{theo-exp}} = 0.999766$. Therefore, the mathematical models explain 99.9933% ($\rho_{\mathrm{cc}}^{\mathrm{theo-exp}^2}$) of the variability of the experimental data in the case of the classic circuit and 99.9532% ($\rho_{\mathrm{pc}}^{\mathrm{theo-exp}^2}$) of the variability of the data in the case of the proposed circuit.

The above shows that both models serve to predict the experimental data with a very strong degree of fit. In the case of the classic circuit, this result was to be expected because it is a simple, well-known circuit. However, it is important to highlight that, in the case of the proposed circuit, this result had to be proved because it is a novel photometer circuit.

IV. DISCUSSION

In the electronic configuration shown in Fig. 3(b), the linearity of the photodiode is maximized. However, when the input signal is corrupted by random-noise signals, for example, by a white-noise signal, the output of the circuit is greatly affected by this unwanted input information. It is well known that, in laboratory experiments, where all conditions are under control, it is very rare for the development engineer to face extreme situations. Nevertheless, in real-life applications, where the behavior of nature cannot be controlled, the designer has to take into account that the designed electronic circuit has to be able to reject disturbances. In other words, the circuit has to be robust against unwanted input signals.

The aforementioned served as a starting point to try to improve the rejection of AWGN input disturbances that corrupt the performance of the photovoltaic mode photodiode amplifier.

In this research, a coefficient (called the relative proximity coefficient) was created whose value served to quantify how far the response of the photometer circuit is from the response that this circuit would have if the input was not corrupted by noise. Therefore, to test the noise rejection of both the classic photometer circuit and the proposed photometer circuit, an AWGN signal was generated by using the Agilent 33120A 15-MHz function/arbitrary waveform generator, and this signal was used to contaminate the photocurrent of the BPW21 in both circuits. Fig. 15 showed that the noise rejection ability of the proposed circuit was better than the one of the classic circuit.

This result was to be expected because the classic photometer circuit is utterly linear. Specifically, the output of this circuit is the superposition of the individual contribution of each of the input signals, and this contribution is given by the convolution between the impulse response of the linear system (i.e., the classic photometer circuit) and each of the input signals [39]. Therefore, in this research, it was decided to solve the problem raised by creating a piecewise linear circuit that, taking advantage of the feedback, would ensure that the relationship between the input and output signals of this new circuit was linear. This circuit was shown in Fig. 5.

Fortunately, the value of the relative proximity coefficient clearly proved that the proposed electronic design successfully rejected the contribution of input disturbances. The results shown in Fig. 15 are in full agreement with the remark made at the end of Section III-C.

Another test that was carried out on both circuits, at the electronic simulation level, was the verification of the behavior of both against variations in the ambient temperature. The result of this test showed that the simpler circuit (i.e., the classic one) was less affected by variations in ambient temperature than the more complex circuit (i.e., the proposed one). However, it is

worth noting that the response of both circuits tends to be very little affected by variations in ambient temperature, this being a satisfactory result.

The reality is that the implementation of the proposed circuit is more complex than that of the classic circuit. However, the proposed circuit is also easy to implement and can be put into practice using inexpensive electronic components. Therefore, in the opinion of the authors of this article, in applications where measurement precision and noise rejection are primordial needs, it is worth using the proposed photometer circuit or some variant of it.

Finally, to verify that the mathematical model proposed for each circuit was able of explaining the variability of the data, the theoretical results were compared against the experimental results. This comparison showed that both proposed models serve to predict the experimental data with a very strong degree of fit. At this point, it is worth mentioning that the mathematical model of the classic circuit is simple and very well known. However, in this sense, the contribution of this article is that a mathematical model for the proposed novel circuit has been presented.

V. Conclusion

In this article, the design of a piecewise linear photometer circuit that takes advantage of feedback to ensure that its output response is linear has been presented. This circuit was shown to have a greater rejection to input AWGN signals than the classic photometer circuit based on a transimpedance amplifier that was used to make the comparison. Furthermore, the linearity of the proposed circuit is only slightly lower than that of the classic circuit, the cost of implementing this circuit is not high, and its assembly is simple.

The aforementioned leads to establishing a tradeoff between greater complexity but greater noise rejection and greater simplicity but lower noise rejection. As the real-life applications of sensing devices are not in places where development and innovation engineers can control the behavior of all the environment variables, it is recommended to take into account this type of electronic circuit design that sacrifices a little complexity to gain great benefits in terms of noise and disturbance rejection.

This research paves the way for others in which piecewise linear circuits can make the most of feedback to perform better than the utterly linear ones in real-life applications.

Appendix
Inverse Laplace Transform of $H(s)$

Let the transfer function of a linear time-invariant system be given by (27), with $A, B, C, D \in \mathbb{R}$, $A \neq 0$, and $B \neq 0$. Then, as a consequence of the fundamental theorem of algebra [40], [41], the denominator of $H(s)$ has three roots, which could be either: 1) three real roots or 2) one real root and two complex conjugate roots. Moreover, the real roots can be repeated

$$H(s) = \frac{A}{Bs^3 + Cs^2 + Ds + 1}. \tag{27}$$

In what follows, the method of the Heaviside formulas will be used to perform the partial fraction decomposition [42] of (27).

A. All the Roots of the Denominator Are Different and of Multiplicity One

Let us assume that the roots of

$$Bs^3 + Cs^2 + Ds + 1$$

are $\alpha_1, \alpha_2, \alpha_3 \in \mathbb{R}$ and $\alpha_1 \neq \alpha_2 \neq \alpha_3$. Then,

$$H(s) = \frac{A}{(s-\alpha_1)(s-\alpha_2)(s-\alpha_3)}$$
$$H(s) = \frac{a_1}{s-\alpha_1} + \frac{a_2}{s-\alpha_2} + \frac{a_3}{s-\alpha_3} \tag{28}$$

where

$$\lim_{s\to\alpha_1}(s-\alpha_1)H(s) = \frac{A}{(\alpha_1-\alpha_2)(\alpha_1-\alpha_3)} = a_1$$
$$\lim_{s\to\alpha_2}(s-\alpha_2)H(s) = \frac{A}{(\alpha_2-\alpha_1)(\alpha_2-\alpha_3)} = a_2$$
$$\lim_{s\to\alpha_3}(s-\alpha_3)H(s) = \frac{A}{(\alpha_3-\alpha_1)(\alpha_3-\alpha_2)} = a_3.$$

Therefore,

$$h(t) = \mathcal{L}^{-1}\{H(s)\}(t)$$
$$h(t) = A\left[\mathcal{L}^{-1}\left(\frac{a_1}{s-\alpha_1}\right) + \mathcal{L}^{-1}\left(\frac{a_2}{s-\alpha_2}\right) + \mathcal{L}^{-1}\left(\frac{a_3}{s-\alpha_3}\right)\right]$$
$$h(t) = A\left[a_1 e^{\alpha_1 t} + a_2 e^{\alpha_2 t} + a_3 e^{\alpha_3 t}\right] \tag{29}$$

where $\mathcal{L}^{-1}$ denotes the inverse Laplace transform.

1) All Roots of the Denominator Are Real and One Is Repeated Twice: Let us assume that the roots of

$$Bs^3 + Cs^2 + Ds + 1$$

are $\alpha_1, \alpha_2, \alpha_3 \in \mathbb{R}$ and $\alpha_1 \neq \alpha_2 = \alpha_3$. Then,

$$H(s) = \frac{A}{(s-\alpha_1)(s-\alpha_2)^2}$$
$$H(s) = \frac{a_1}{s-\alpha_1} + \frac{a_2}{s-\alpha_2} + \frac{a_3}{(s-\alpha_2)^2} \tag{30}$$

where the following holds.

1) $\lim_{s\to\alpha_1}(s-\alpha_1)H(s) = A/(\alpha_1-\alpha_2)^2 = a_1$.
2) $\lim_{s\to\alpha_2}(s-\alpha_2)^2 H(s) = A/(\alpha_2-\alpha_1) = a_3$.
3) By multiplying (29) by $(s-\alpha_2)^2$, it is obtained that

$$\frac{A}{s-\alpha_1} = \frac{a_1(s-\alpha_2)^2}{s-\alpha_1} + a_2(s-\alpha_2) + a_3.$$

Therefore, finding the derivative of both sides of the previous equation, it is obtained that

$$\frac{-A}{(s-\alpha_1)^2} = \frac{2a_1(s-\alpha_1)(s-\alpha_2) - a_1(s-\alpha_2)^2}{(s-\alpha_1)^2} + a_2$$

and

$$\lim_{s\to\alpha_2}\frac{-A}{(s-\alpha_1)^2} = \frac{-A}{(\alpha_2-\alpha_1)^2}$$
$$\lim_{s\to\alpha_2}\frac{2a_1(s-\alpha_1)(s-\alpha_2)-a_1(s-\alpha_2)^2}{(s-\alpha_1)^2} + a_2 = a_2.$$

As a result of the above, it can be seen that $a_2 = -A/(\alpha_2-\alpha_1)^2$.

Finally,

$$h(t) = A\left[\mathcal{L}^{-1}\left(\frac{a_1}{s-\alpha_1}\right) + \mathcal{L}^{-1}\left(\frac{a_2}{s-\alpha_2}\right) + \mathcal{L}^{-1}\left(\frac{a_3}{(s-\alpha_2)^2}\right)\right]$$
$$h(t) = A\left[a_1 e^{\alpha_1 t} + a_2 e^{\alpha_2 t} + a_3 t e^{\alpha_2 t}\right]. \quad (31)$$

2) All Roots of the Denominator Are Real and Equal: Let us assume that the roots of

$$Bs^3 + Cs^2 + Ds + 1$$

are $\alpha_1, \alpha_2, \alpha_3 \in \mathbb{R}$ and $\alpha_1 = \alpha_2 = \alpha_3$. Then,

$$H(s) = \frac{A}{(s-\alpha_1)^3} \quad (32)$$

and

$$h(t) = \mathcal{L}^{-1}\left(\frac{A}{(s-\alpha_1)^3}\right) = A e^{\alpha_1 t}\frac{t^2}{2}. \quad (33)$$

3) Denominator Has Complex Conjugate Roots: Let us assume that the roots of

$$Bs^3 + Cs^2 + Ds + 1$$

are α_1 and $\alpha_2 \pm j\beta_2$, where $\alpha_1, \alpha_2, \beta_2 \in \mathbb{R}$, $\beta_2 \neq 0$, and $j = \sqrt{-1}$. Then,

$$H(s) = \frac{A}{(s-\alpha_1)\left[(s-\alpha_2)^2 + \beta_2^2\right]}$$
$$H(s) = \frac{a_1}{s-\alpha_1} + \frac{a_2(s-\alpha_2) + a_3}{(s-\alpha_2)^2 + \beta_2^2} \quad (34)$$

where the following holds.

1) $\lim_{s\to\alpha_1}(s-\alpha_1)H(s) = A/((\alpha_1-\alpha_2)^2 + \beta_2^2) = a_1$.
2) By multiplying (34) by $(s-\alpha_2)^2 + \beta_2^2$ and substituting $s = \alpha_2 + j\beta_2$, it is obtained that

$$\frac{A}{\alpha_2 + j\beta_2 - \alpha_1} = a_2(\alpha_2 + j\beta_2 - \alpha_2) + a_3$$
$$A\frac{\alpha_2 - \alpha_1 - j\beta_2}{(\alpha_2-\alpha_1)^2 + \beta_2^2} = j\beta_2 a_2 + a_3.$$

Therefore,

$$a_2 = \frac{-A}{(\alpha_2-\alpha_1)^2 + \beta_2^2}$$
$$a_3 = \frac{A(\alpha_2-\alpha_1)}{(\alpha_2-\alpha_1)^2 + \beta_2^2}.$$

Finally,

$$h(t) = A\left[\mathcal{L}^{-1}\left(\frac{a_1}{s-\alpha_1}\right) + \mathcal{L}^{-1}\left(\frac{a_2(s-\alpha_2)}{(s-\alpha_2)^2 + \beta_2^2}\right)\right] + A\left[\mathcal{L}^{-1}\left(\frac{a_3}{(s-\alpha_2)^2 + \beta_2^2}\right)\right]$$
$$h(t) = A\left[a_1 e^{\alpha_1 t} + a_2 e^{\alpha_2 t}\cos(\beta_2 t) + a_3\frac{e^{\alpha_2 t}\sin(\beta_2 t)}{\beta_2}\right]. \quad (35)$$

REFERENCES

[1] M. Johnson, *Photodetection and Measurement: Maximazing Performance in Optical Detection Systems*. New York, NY, USA: McGraw-Hill, 2003.

[2] M. Norgia, A. Magnani, D. Melchionni, and A. Pesatori, "Drop measurement system for biomedical application," *IEEE Trans. Instrum. Meas.*, vol. 64, no. 9, pp. 2513–2517, Sep. 2015.

[3] L. Lombardo, M. Parvis, E. Angelini, and S. Grassini, "An optical sampling system for distributed atmospheric particulate matter," *IEEE Trans. Instrum. Meas.*, vol. 68, no. 7, pp. 2396–2403, Jul. 2019.

[4] Z. Yang, G. Li, R. Yan, Y. Sun, L.-A. Wu, and A.-X. Zhang, "3-D computational ghost imaging with extended depth of field for measurement," *IEEE Trans. Instrum. Meas.*, vol. 68, no. 12, pp. 4906–4912, Dec. 2019.

[5] D. V. Vladutescu *et al.*, "Remote sensing instruments used for measurement and model validation of optical parameters of atmospheric aerosols," *IEEE Trans. Instrum. Meas.*, vol. 61, no. 6, pp. 1733–1746, Jun. 2012.

[6] K. Uehira, K. Suzuki, and H. Ikeda, "Does optoelectronic watermark technology migrate into business and industry in the near future? Applications of optoelectronic watermarking technology to new business and industry systems utilizing flat-panel displays and smart devices," *IEEE Trans. Ind. Appl.*, vol. 52, no. 1, pp. 511–520, Jan. 2016.

[7] P. Predeep, *Optoelectronics: Devices and Applications*. Rijeka, Croatia: InTech, 2011.

[8] J. G. Graeme, *Photodiode Amplifiers: OP AMP Solutions*. New York, NY, USA: McGraw-Hill, 1996.

[9] R. Pallàs-Areny and J. G. Webster, *Sensors and Signal Conditioning*, 2nd ed. New York, NY, USA: Hoboken, NJ, USA: Wiley, 2001.

[10] B. Razavi, "The transimpedance amplifier [a circuit for all seasons]," *IEEE Solid State Circuits Mag.*, vol. 11, no. 1, pp. 10–97, Winter 2019.

[11] J. I. Civera, I. R. Gil, N. Laguarda-Miro, E. Garcia-Breijo, L. Gil-Sánchez, and R. Martínez-Guijarro, "Instrument for sunlight extinction measurement in water bodies," *Sens. Actuators A, Phys.*, vol. 168, no. 2, pp. 267–274, Aug. 2011.

[12] D. Nordin and K. Hyypa, "Single-stage photodiode op-amp solution suited for a self-mixing FMCW system," *IEEE Trans. Instrum. Meas.*, vol. 52, no. 6, pp. 1820–1824, Dec. 2003.

[13] P. Wright, K. B. Ozanyan, S. J. Carey, and H. McCann, "Design of high-performance photodiode receivers for optical tomography," *IEEE Sensors J.*, vol. 5, no. 2, pp. 281–288, Apr. 2005.

[14] R. Yun and V. J. Koomson, "A novel CMOS frequency-mixing transimpedance amplifier for frequency domain near infrared spectroscopy," *IEEE Trans. Circuits Syst. I, Reg. Papers*, vol. 60, no. 1, pp. 84–94, Jan. 2013.

[15] M. Moreira *et al.*, "A low-cost NIR digital photometer based on InGaAs sensors for the detection of milk adulterations with water," *IEEE Sensors J.*, vol. 16, no. 10, pp. 3653–3663, May 2016.

[16] M. Moreira, A. L. de Souza Madureira Felício, and J. A. de França, "Calibration of a photometer for quantification of ethanol in gasoline: Absorbance determination," *IEEE Trans. Instrum. Meas.*, vol. 67, no. 9, pp. 2119–2128, Sep. 2018.

[17] H. Zheng, R. Ma, M. Liu, and Z. Zhu, "A linear dynamic range receiver with timing discrimination for pulsed TOF imaging LADAR application," *IEEE Trans. Instrum. Meas.*, vol. 67, no. 11, pp. 2684–2691, Nov. 2018.

[18] L. da Silva Dias, J. C. da Silva Junior, A. L. de Souza Madureira Felício, and J. A. de França, "A NIR photometer prototype with integrating sphere for the detection of added water in raw milk," *IEEE Trans. Instrum. Meas.*, vol. 67, no. 12, pp. 2812–2819, Dec. 2018.

[19] A. Papoulis and S. U. Pillai, *Probability, Random Variables, and Stochastic Processes*, 4th ed. New York, NY, USA: McGraw-Hill, 2002.

[20] S. V. Vaseghi, *Advanced Digital Signal Processing and Noise Reduction*, 4th ed. Chichester, U.K.: Wiley, 2008.

[21] P. Regtien and E. Dertien, *Sensors for Mechatronics*, 2nd ed. Cambridge, MA, USA: Elsevier, 2018.

[22] S. Song, J. Y. Jang, Y. J. Hwang, M. S. Kim, and Y. S. Choi, "Real-time abnormal-signal detection under a noisy environment using a resonance filter," *IEEE Trans. Instrum. Meas.*, vol. 70, pp. 1–8, 2021.

[23] C. L. Ng, M. B. I. Reaz, and M. E. H. Chowdhury, "A low noise capacitive electromyography monitoring system for remote healthcare applications," *IEEE Sensors J.*, vol. 20, no. 6, pp. 3333–3342, Mar. 2020.

[24] W. Hernandez, "Photometer circuit based on positive and negative feedback compensations," *Sensor Lett.*, vol. 5, no. 3, pp. 612–614, Sep. 2007.

[25] W. Hernandez, "Linear robust photometer circuit," *Sens. Actuators A, Phys.*, vol. 141, no. 2, pp. 447–453, Feb. 2008.

[26] W. Hernandez, "Performance analysis of a robust photometer circuit," *IEEE Trans. Circuits Syst. II, Exp. Briefs*, vol. 55, no. 2, pp. 106–110, Feb. 2008.

[27] *BPW21 Datasheet (PDF)—OSRAM GmbH*. Accessed: Nov. 4, 2021. [Online]. Available: https://www.alldatasheet.com/datasheet-pdf/pdf/1019713/OSRAM/BPW21.html

[28] *TL08xx FET-Input Operational Amplifiers (Rev. L)*. Accessed: Nov. 4, 2021. [Online]. Available: https://www.ti.com/document-viewer/TL084/datasheet/GUID-E27A13E7-9983-4E1A-B8A3-32C7736B4741#TITLE-SLOS081SLOS0814121
[29] *Proteus*. Accessed: Nov. 4, 2021. [Online]. Available: https://www.labcenter.com/
[30] V. D. Wangkheirakpam, B. Bhowmick, and P. D. Pukhrambam, "Modeling and simulation of optically gated TFET for near infra-red sensing applications and its low frequency noise analysis," *IEEE Sensors J.*, vol. 20, no. 17, pp. 9787–9795, Sep. 2020.
[31] A. Depari *et al.*, "Autobalancing analog front end for full-range differential capacitive sensing," *IEEE Trans. Instrum. Meas.*, vol. 67, no. 4, pp. 885–893, Apr. 2018.
[32] X. Wei, T. Nagashima, M. K. Kazimierczuk, H. Sekiya, and T. Suetsugu, "Analysis and design of class-E_M power amplifier," *IEEE Trans. Circuits Syst. I, Reg. Papers*, vol. 61, no. 4, pp. 976–986, Apr. 2014.
[33] *MATLAB*. Accessed: Nov. 4, 2021. [Online]. Available: https://www.mathworks.com/products/MATLAB.html
[34] G. C. Canavos, *Applied Probability and Statistical Methods*, 1st ed. Boston, MA, USA: Little, Brown and Company, 1984.
[35] *EAGLE*. Accessed: Nov. 11, 2021. [Online]. Available: https://www.autodesk.com/products/eagle/overview
[36] *Newenergy Data Sheet*. Accessed: Nov. 11, 2021. [Online]. Available: https://www.mouser.com/datasheet/2/810/NewEnergy_StarBoard_Modules_DataSheet-2326290.pdf
[37] *JCGM 200:2012 International Vocabulary of Metrology—Basic and General Concepts and Associated Terms (VIM)*. Accessed: Dec. 28, 2021. [Online]. Available: https://www.bipm.org/documents/20126/2071204/JCGM_200_2012.pdf/f0e1ad45-d337-bbeb-53a6-15fe649d0ff1
[38] R. M. Kaplan and D. P. Saccuzzo, *Psychological Testing: Principles, Applications, and Issues*, 9th ed. Boston, MA, USA: Cengage Learning, 2018.
[39] A. V. Oppenheim, A. S. Willsky, and H. Nawab, *Signals & Systems*, 2nd ed. Upper Saddle River, NJ, USA: Prentice-Hall, 1997.
[40] G. Birkhoff and S. Mac Lane, *A Survey of Modern Algebra*, 5th ed. Natick, MA, USA: A K Peters, 1997.
[41] J. Ward Brown and R. V. Churchill, *Complex Variables and Applications*, 8th ed. New York, NY, USA: McGraw-Hill, 2009.
[42] E. Kreyszig, *Advanced Engineering Mathematics*, 9th ed. New York, NY, USA: Wiley, 2006.

Wilmar Hernandez (Senior Member, IEEE) received the Electronics Engineering degree and the specialist degree in microelectronics from the Instituto Superior Politecnico Jose Antonio Echeverria (ISPJAE), Havana, Cuba, in 1992 and 1994, respectively, and the M.S. degree in signal treatment and the Ph.D. degree in electronic engineering from Enginyeria La Salle, Universitat Ramon Llull, Barcelona, Spain, in 1997 and 1999, respectively.

From 1992 to 1995, he was a Lecturer with the Electrical Engineering Faculty, ISPJAE, where he was a Researcher with the Microelectronics Research Center. From 1999 to 2003, he was with the Department of Electronics and Instrumentation, University Institute for Automobile Research, Universidad Politécnica de Madrid (UPM), Madrid, Spain, where he was the Technical Director from January 2003 to January 2004. From January 2004 to March 2013, he was an Associate Professor of circuits and systems with the Department of Circuits and Systems, EUIT de Telecomunicacion, UPM. From September 2014 to September 2015, he was a Researcher with SENESCYT, Azogues, Ecuador, under the Prometeo Fellowship Program. From December 2015 to November 2017, he was a Professor with the Universidad Técnica Particular de Loja, Loja, Ecuador. Since January 2018, he has been a Professor with the Universidad de Las Américas, Quito, Ecuador.

Alfredo Mendez was born in Madrid, Spain, in June 1958. He received the bachelor's degree in mathematical sciences (area of fundamental mathematics), the M.S. degree in mathematical sciences and the Ph.D. degree in mathematical sciences (area of statistics and operational research) from the Universidad Complutense de Madrid (UCM), Madrid, in 1981, 1987, and 1995, respectively.

From 1983 to 1993, he was a Lecturer with the EUIT Agricola, Universidad Politécnica de Madrid (UPM), Madrid. Since 1993, he has been an Associate Professor of mathematics with the Departamento de Matematica Aplicada a las Tecnologias de la Informacion y Comunicaciones (DMATIC), ETSIS de Telecomunicacion, Universidad Politécnica de Madrid, where he was the Director from May 2004 to May 2012.

Vicente González-Posadas was born in Madrid, Spain, in 1968. He received the B.S. degree in radio communication engineering from the Universidad Politécnica de Madrid (UPM), Madrid, in 1992, the M.S. degree in physics from the Universidad Nacional de Educacion a Distancia, Madrid, in 1995, the M.S. degree in high strategic studies from CESEDEN, Madrid, in 2009, and the Ph.D. degree in telecommunication engineering from the Universidad Carlos III de Madrid, Madrid, in 2001.

He is currently a Full Professor with the ETSIS de Telecomunicacion, UPM. He has authored or coauthored over 60 technical conferences, letters, and journal articles. His current research interests include active antennas, microstrip antennas, composite right/left-handed (CRLH) lines and metamaterials, microwave technology, and radio-frequency identification (RFID).

José Luis Jiménez-Martín was born in Madrid, Spain, in 1967. He received the B.S. degree in electrical engineering with a minor in radio communication engineering, the M.S. degree in telecommunications engineering, and the Ph.D. degree from the Universidad Politécnica de Madrid (UPM), Madrid, in 1991, 2000, and 2005, respectively, and the M.S. degree in high strategic studies from CESEDEN, Madrid, in 2007.

He is currently an Associate Professor with the ETSIS de Telecomunicacion, UPM. He has authored or coauthored over 60 technical conferences, letters, and journal articles. His current research interests include oscillators, amplifiers, and microwave technology.

Francisco José Arqués-Orobón was born in Murcia, Spain, in 1966. He received the B.S. degree in electrical engineering with a minor in telematics engineering from the Universidad Politécnica de Madrid (UPM), Madrid, Spain, in 1992, the M.S. degree in electrical engineering from the Universidad Complutense de Madrid, Madrid, in 2002, and the Ph.D. degree from UPM in 2016.

From 1993 to 2001, he worked in the Spanish Ministry of Environment within a technological project funded by the European Union aimed at monitoring and quality control of waters, where automatic stations of measurement of diverse parameters were developed and whose data are sent via satellite (VSAT). In 2003, he earned a position of University School Professor (tenured) at UPM, where he earned a position of Associate Professor (full-time) in 2017. He is currently with the Research Group on Electromagnetism, Microwave and Radio Frequency Antennas (DIEMAG), UPM. Since 2004, he has been the leader of more than 20 projects with public and private entities, focused on detection, monitoring, and data processing.